Research Article Vol. 56, No. 28 / /Applied Optics 1

applied optics

# Adaptive optics retinal imaging with automatic detection of the pupil and its boundary in real time using Shack–Hartmann images

Alberto de Castro,* Lucie Sawides, Xiaofeng Qi, and Stephen A. Burns

School of Optometry, Indiana University, 800 E. Atwater Ave, Bloomington, Indiana 47401, USA
*Corresponding author: alberto@indiana.edu

Received 13 April 2017; revised 12 July 2017; accepted 19 July 2017; posted 20 July 2017 (Doc. ID 292377); published 0 MONTH 0000

**Retinal imaging with an adaptive optics (AO) system usually requires that the eye be centered and stable relative to the exit pupil of the system. Aberrations are then typically corrected inside a fixed circular pupil. This approach can be restrictive when imaging some subjects, since the pupil may not be round and maintaining a stable head position can be difficult. In this paper, we present an automatic algorithm that relaxes these constraints. An image quality metric is computed for each spot of the Shack–Hartmann image to detect the pupil and its boundary, and the control algorithm is applied only to regions within the subject's pupil. Images on a model eye as well as for five subjects were obtained to show that a system exit pupil larger than the subject's eye pupil could be used for AO retinal imaging without a reduction in image quality. This algorithm automates the task of selecting pupil size. It also may relax constraints on centering the subject's pupil and on the shape of the pupil.** 

***OCIS codes:*** (010.1080) Active or adaptive optics; (170.0110) Imaging systems; (170.4470) Ophthalmology.

https://doi.org/10.1364/AO.99.099999

## 1. INTRODUCTION

Adaptive optics (AO) correction of the aberrations of the eye to obtain high-resolution images of the retina was first demonstrated in a flood illuminated system [1] and was soon combined with scanning laser ophthalmoscopy [2], time domain optical coherence tomography (OCT) [3], and spectral domain OCT [4]. The main components of an AO system typically include a wavefront sensor, a wavefront corrector, and a control algorithm. In most retinal imaging systems, the wavefront sensor is a Shack–Hartmann (SH) type, and the wavefront corrector is a deformable mirror (DM). The purpose of the control algorithm is to use the information measured by the wavefront sensor to calculate the signal that is sent to the corrector. While in astronomical applications, the control algorithm uses knowledge of the statistics of the time-varying source of aberrations, atmospheric turbulence, this is not the case in retinal imaging AO systems, where the control algorithm is usually an integral controller.

There are several problems that arise in maintaining wavefront control during AO retinal imaging. Improved control structures, such as using a Smith predictor [5], a tuned adaptive controller [6], or a waffle or Kolmogorov's model penalty [7] have been proposed in the literature, but it is not clear which is the best strategy to apply, especially in clinical applications where AO imaging in some patients can be challenging due to high aberrations, irregular pupils, and eye movements.

Typically, an active control loop is used to correct dynamics in the aberrations themselves. However, eye movements can also generate temporal variations in the wavefront control, since movements of the eye in relation to the AO correction can cause changes in the required AO correction due to shifts in the aberration pattern and changes in aberrations with visual angle. Eye movements have been addressed by systems that correct the pupil position on the fly [8]. While an eye tracker can be coupled to the imaging system, some studies have demonstrated that the SH images can be used to track the pupil position either by measuring the overall centroid of the whole aberrometric image [9] or fitting an ellipse to the illuminated lenslets [10].

In all of these approaches, the measurement of the wavefront at the pupil boundary is not precise because the SH lenslets of the corresponding positions are not fully illuminated. Errors at these boundary locations affect the wavefront reconstruction dramatically, even in the measurement of the low-order aberration [11], thus degrading the image quality quickly. Typically, this problem is solved by shrinking the size of the pupil controlled to an area smaller than the subject's pupil size [1]. Some commercial systems are designed to correct the aberrations in

an area smaller than the average pupil size [12]. This smaller size increases the robustness of the system, but resolution would be increased by increasing the system pupil to match each individual's eye pupil. With a system that allowed changing the system control pupil, it was shown that the best image was obtained when the size of the system control was slightly smaller than the pupil of the eye [11]. While this paper used an algorithm to enlarge the controlled area, extrapolating the phase measurements to improve stability, it was still necessary to select the right pupil size and to maintain the subject's pupil position at the correct location.

Most control algorithms are designed to correct the images in an eye with a circular pupil, often of a fixed size during the measurement. However, even with pharmacological dilation, some subjects' pupils can change size or are irregular in their shape due to factors such as cataracts or intraocular lenses. The usual approach when dealing with an irregular sized pupil or imaging very eccentric locations in the retina, where pupil shape is elliptical, is to choose the maximum circle size that fits inside the subject's pupil. Although larger pupils result in better lateral resolution, a smaller pupil that avoids the boundary effects can produce better quality images [11]. However, an algorithm that could dynamically adapt to irregular pupil shapes should improve the image quality in these situations.

Instead of fixing programmatically the area where the aberrations will be measured and corrected, we propose an approach that monitors the wavefront sensor that subtends an area larger than the subject's pupil and uses the SH images to dynamically detect the pupil shape and position. In this paper, we test this approach by defining a metric to quantify the quality of the image formed by each lenslet of a SH sensor and use this metric to detect the shape and location of the pupil, defined as areas that provide reasonable quality spots. Then, using simple neighborhood rules, the algorithm detects the pupil boundary and bases wavefront control on areas within the pupil. The hypothesis is that we can use strategies for adapting to the "missing" slope estimates within the control loop to perform as well as the situation when we use an optimum match between the system pupil and the individual's own pupil. Results with these strategies are compared for both a model eye and the eyes of young, normal subjects.

## 2. METHODS

### A. Imaging System

We collected images with an AO scanning laser ophthalmoscope that has been previously described [13]. Briefly, a laser beam is focused and scanned across the retina in a raster pattern, and the light reflected and scattered from the retina is acquired sequentially with an avalanche photodiode to construct a retinal image. The aberrations are calculated using a custom SH wavefront sensor with microlenses of 0.3 mm diameter (0.375 mm at the eye's pupil). Each lenslet had a 7.6 mm focal length and imaged the retina onto a ~~CCD camera~~ (Uniq Vision Inc. UP-1830CL). In this system, two DMs in a woofer–tweeter configuration (Imagine Eyes MIRAO DM, 52 actuators, and Boston Micromachines MEMS DM, 140 actuators) are used to correct the aberrations of the eye. The eye pupil, the scanners, the two DMs, and the lenslet array of the wavefront sensor are optically conjugated.

The spots formed by the lenslets on the SH camera were searched for within the 45 × 45 pixels area subtended by each lenslet on the CCD. The spot location was calculated using a shrinking-box approach [14] with a two-step algorithm: first the pixel with the highest intensity was located, and then the centroid of the surrounding area (square of 20 × 20 pixels) was calculated.

The images of the model eye were obtained with the typical system configuration whose exit pupil is 8 mm. For the human testing, the pupil of the system was magnified to allow us to test the ability of the algorithm to automatically select the largest available pupil within the SH imaging pupil; we moved the final spherical mirror of the system to expand the system exit pupil to 9.3 mm. This resulted in a slightly smaller retinal scanned area and also changed the system aberrations somewhat, but allowed us to better test the ability of the algorithms when the subject's pupil moved within a larger system pupil.

### B. Lenslet Quality Metric

We defined a metric to estimate the quality of the spot formed by each lenslet on the CCD of the SH to identify those whose conjugated position was inside the subject's pupil. The metric was defined as the ratio between the light in the area close to the centroid (20 × 20 pixels square) and the total intensity over the entire CCD area subtended by each lenslet (45 × 45 pixels square). The spots formed with light reflected from the retina through relatively clear ocular media are focused onto the camera surface, and as a result, the corresponding lenslet will result in a high metric value. In the areas conjugated to positions outside the subject's pupil, or where light is backscattered from the cornea or from lenticular opacities, the SH lenslet will poorly focus the light, resulting in spread of light at the plane of the CCD, and these lenslets will score a low metric value.

A threshold was established to discriminate the areas where lenslets formed concentrated spots. The lenslets whose metric was lower than this threshold were marked as "rejected" and classified for exclusion.

### C. Boundary of the Pupil

Once all of the lenslets were classified for inclusion or exclusion using the spot quality metric, the boundary of the pupil was calculated using neighborhood rules. In the rectangular array of the SH used, each lenslet has eight neighbors. A lenslet was marked as boundary if it had at least two neighboring lenslets marked as rejected, i.e., if at least two neighbor lenses' metric was below the threshold. An example for one of the subjects can be seen in Fig. 1.

### D. Adaptive Optics Control Algorithm

We used a direct slope algorithm [15,16] that attempts to correct the wavefront by zeroing the local slope vector measured by the SH. In the direct slope control~~s~~, a linear relationship is assumed between the movement of the $m$ mirror actuator and the $n$ SH spot displacement in both horizontal and vertical directions with the equation

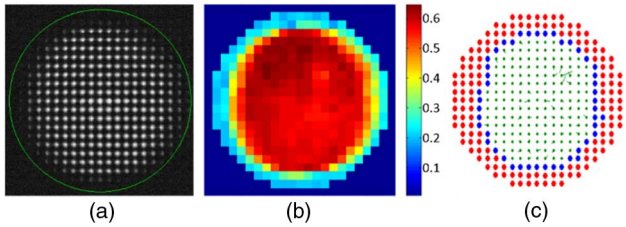


F1:1 **Fig. 1.** (a) CCD image of the Shack–Hartmann wavefront sensor.
F1:2 The green circle indicates the area monitored by the adaptive optics
F1:3 control algorithm. (b) Metric value of all the spots of the image.
F1:4 (c) Lenslets with metric above 0.5 were accepted (in green), and those
F1:5 with metric below 0.5 (in red) or in the pupil boundary (in blue) were
F1:6 marked for rejection. In the last image, the local slope errors for ac-
F1:7 cepted lenslets are drawn as vectors.

$$\begin{pmatrix} s_{1,x} \\ s_{1,y} \\ s_{2,x} \\ s_{2,y} \\ \vdots \\ \vdots \\ s_{n,x} \\ s_{n,y} \end{pmatrix} = \begin{pmatrix} A_{11,x} & A_{12,x} & \cdots & A_{1m,x} \\ A_{11,y} & A_{12,y} & \cdots & A_{1m,y} \\ A_{21,x} & A_{22,x} & \cdots & A_{2m,x} \\ A_{21,y} & A_{22,y} & \cdots & A_{2m,y} \\ \vdots & \vdots & \ddots & \vdots \\ \vdots & \vdots & \ddots & \vdots \\ A_{n1,x} & A_{n2,x} & \cdots & A_{nm,x} \\ A_{n1,y} & A_{n2,y} & \cdots & A_{nm,y} \end{pmatrix} \begin{pmatrix} m_1 \\ m_2 \\ \vdots \\ m_m \end{pmatrix},$$

where $A_{ii,x}$ and $A_{ij,y}$ are the influence of the actuator $j$ on the components $x$ and $y$ of the spot $i$. To calculate actuator commands with each measurement of slopes obtained with the SH, the inverse relationship is needed, and a pseudoinverse is typically computed using a singular value decomposition. However, the direct use of the pseudoinverse, $m = A^{+}s$, is often not stable, and typically some modes are removed [7,17] or muffled using a damped least-squares approach [18,19]:

$$m = (A^T A + \lambda I)^{-1} A^T s.$$

The resulting matrix that is used to calculate the actuator commands with the slopes measured in the SH, $m = Cs$ is known as the control matrix [20]. In our case, we used a Lagrange multiplier to combine the two mirrors into a single control matrix [19,21], which provides a damped least-squares error control.

### E. Processing of Rejected Lenslets

In this study, we compared two approaches to deal with rejected lenslets within the AO control loop. The first approach, referred to as "zeroing rejected," is to set the slope of the rejected lenslets such that there is no need to change the DM, i.e., set $s_{i,x} = 0$ and $s_{i,y} = 0$ for lenslet $i$, if it is rejected. This approach then calculates the actuator command using the same control matrix during the whole imaging session. Zeroing the slopes removes what may be noisy measurements, improving system stability. However, this operation may impose constraints on nearby areas of the DM, since the finite size of the influence function of each mirror actuator will cause them to balance the apparently perfect wavefront outside the pupil with errors inside the pupil. After zeroing the slopes of the rejected lenslets, we smoothed the transition between the area with valid measurements and the area where the slopes had been set to zero by applying a $2 \times 2$ median filter to the rejected lenslets' slopes, providing a transition to the area of zeros, but leaving accepted lenslet errors unchanged.

We refer to the second approach as "removing rejected." This approach removes the rejected lenslets from the vector of slopes and from the corresponding rows of the influence matrix, i.e., eliminates $s_{i,x}$, $s_{i,y}$ and $A_{ij,x}$ and $A_{ij,y}$ for $j = 1, 2, \ldots, m$, if the lenslet $i$ is rejected. With this approach, a new control matrix has to be calculated after each SH image acquisition. By recalculating the control matrix without the rows corresponding to rejected lenslets, we eliminate the influence of these positions and effectively allow the control to act on only non-rejected lenslets. Even with the rows deleted, the system of equations will not be underdetermined for reasonable pupil sizes, since in the AO systems used for ophthalmological applications, the number of SH spots is usually larger than the number of actuators [16]. The algorithm to perform these calculations in each iteration (remove the rows of influence matrix and calculate the control matrix with the damped least-squares method) was programmed in C++ with Eigen [22].

### F. Data Collection in Model Eye and Healthy Subjects

To test the performance of these algorithms in the absence of eye movements, we imaged a model eye composed of an 80-mm focal length lens and a printed paper target. The physical pupil diameter of the model eye was set to 6 mm, which corresponded to $16 \times 16$ lenslets in the SH plane. The control pupil, i.e., the region of the SH sensor available for the computation of slopes, was varied between 4.2 and 7.9 mm ($11 \times 11$ to $21 \times 21$ lenslets on the SH plane, respectively), and sequences of 100 video frames covering a $2 \times 2$ degree region of the paper target were collected.

The AO corrected image quality was calculated as the average intensity of the images obtained about 15 s after starting the AO loop when the mirror position had converged on its final value. The convergence speed was estimated as the change in the intensity of the video frames with time after AO control was initiated. A sigmoid function of time was fit to the measured intensities, and the time to a value corresponding to 90% of the final intensity was used as a measure of convergence speed.

In five young healthy subjects whose pupils were dilated with one drop of 1% tropicamide, images of the cone photoreceptor layer of the retina were obtained at 2, 5, and 9 deg eccentricity. Three short videos (100 frames, 3 s) were obtained at each retinal location. Images of the system controlling a pupil larger than those of the subjects were collected with the two approaches described previously for the model eye. The results were compared to a more standard approach, commonly used in AO retinal imaging systems, which restricts the control pupil size to be slightly smaller than the subject's pupil [23].

The captured videos were processed using software written in MATLAB (The Mathworks, Natick, Massachusetts). Essentially the eye movements were removed from the images aligning the frames with a reference frame, and a video with a

stable image of the retina was created. The same area of the image of the retina, of around 1 × 1 deg without blood vessels, was located in all the videos, and the image quality in terms of both average intensity and integrated power contained under the Fourier transform (FT) of the image up to the diffraction limit, omitting the DC power, 135 cycles per deg, was calculated in the selected area for each frame in the video and averaged.

## 3. RESULTS

A fixed lenslet metric threshold of 0.5 was sufficient to detect the pupil in both the model eye and all human subjects. The quality metric of the lenslets conjugated with points inside the pupil was approximately 0.6–0.7, and the quality metric of the lenslets outside the pupil of the subject was about 0.2–0.3.

### A. Image Quality in the Model Eye

The average intensity of the final images varied with the size of the control pupil and the algorithm (Fig. 2). As expected, when controlling pupils smaller than the pupil of the model eye, the image quality increased with increasing control pupil size. However, when the control pupil was larger than the model eye pupil, the image quality dropped dramatically when all the SH spots were used. Applying the modified control algorithm where lenslets that did not meet the metric criterion were rejected eliminated this drop in image quality. There was no difference in terms of image quality between zeroing the slopes of the rejected lenslets and removing their information from the influence matrix.

### B. Convergence in the Model Eye

Convergence time was approximately constant for the small control pupils, but was quite variable, perhaps due to the smaller number of lenslets contributing to the control. However, convergence time varied depending on the control algorithm for control regions larger than the eye's pupil (Fig. 3). For larger control areas, removing the spots from the influence matrix maintained the convergence time, but zeroing the slopes of the rejected lenslets was slower.

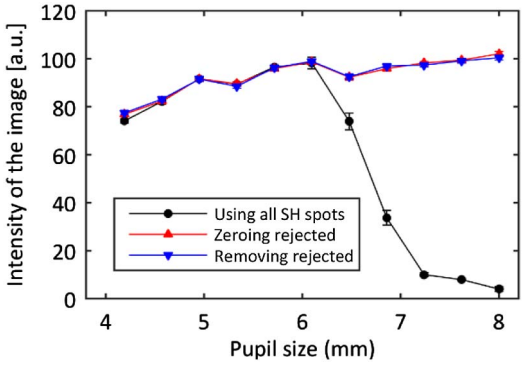


**Fig. 2.** Final intensity of the model eye images as a function of the control pupil size for each of the control algorithms. If all the SH spots are used to control the AO loop, the best practice is to choose a pupil slightly smaller than the eye pupil, since the misinformation from areas outside the eye pupil decreases the image quality. When the rejected spots are excluded, the image quality is maintained, even when controlling pupil sizes larger than the eye's pupil, which was 6 mm. The error bars represent the standard deviation of three repeated measurements.

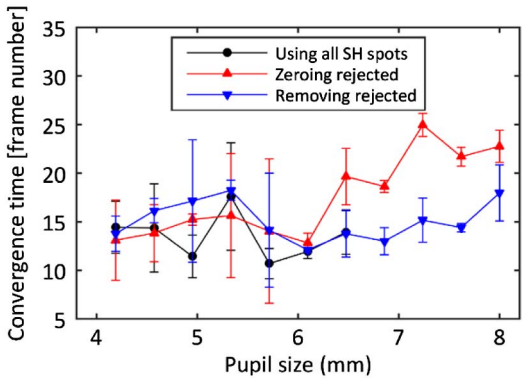


**Fig. 3.** Convergence time estimated as the time elapsed between the initiation of the adaptive optics algorithm and the moment when the intensity on the images is 90% of the final intensity. The error bars represent the standard deviation of three repeated measurements.

### C. Automatic Pupil Selection and Image Quality in Subjects

The metric threshold algorithm selected an area of the SH image that visually corresponded to the area of the pupil in the SH images (Fig. 4). To visualize the results of the algorithm, the lenslets with lenslet quality metrics below the threshold value were marked as rejected with red color, and within the unmarked lenslets, the edge was identified and marked as blue spots. While the images were recorded, changes in the pupil size of the subject as well as blinks were detected in real time (see Visualization 1).

The diameter of the pupil of the subjects following dilation ranged from 6.5 to 8 mm, which corresponded to 16 × 16 and 18 × 18 lenslets, respectively. The average image quality of the frames of the video captured using the proposed algorithms (setting the slope of the rejected lenslets to zero and removing the corresponding rows from the influence matrix) was compared with the average image quality of the video recorded

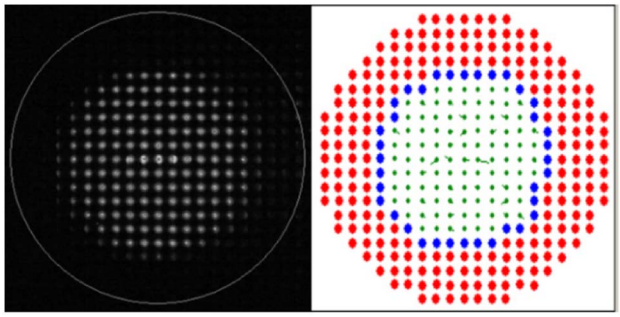

**Fig. 4.** Raw SH image (left) with a circle indicating the area of the system pupil subtended by the AO system and processed image (right) where the rejected lenslets are marked in red, and the lenslets identified as pupil boundary are marked in blue. For the accepted lenslets (green), the residual slopes are plotted as vectors. Changes in pupil position, pupil size, and blinks were detected in real time (see Visualization 1).

using a fixed pupil of a size slightly smaller than the subject's pupil. Figure 5 shows the average of the ratio of intensities and frequency content for the three locations on each subject, as well as the average across subjects for the two approaches. Values for the restricted pupil condition were used to normalize each subject's reflectance and thus were all 1.0.

A ratio less than 1 would indicate that the new approaches did not generate better image quality than was obtained when using the standard algorithm. The average ratio value was not significantly different from 1 for any individual subject; however, on average, image quality was slightly improved with the metric-based control. The average intensity ratio for zeroing rejected lenslets and applying the median filter to transition across the pupil edge was $1.06 \pm 0.08$ and for removing rejected lenslets from the control algorithm was $1.03 \pm 0.09$. The average frequency content ratio was $1.01 \pm 0.03$ for both the zeroing rejected and removing rejected lenslets approach. The difference between the two algorithms in terms of average image quality was not significant. Due to blinks and eye motions, the convergence times for the human subjects were variable and were not analyzed.

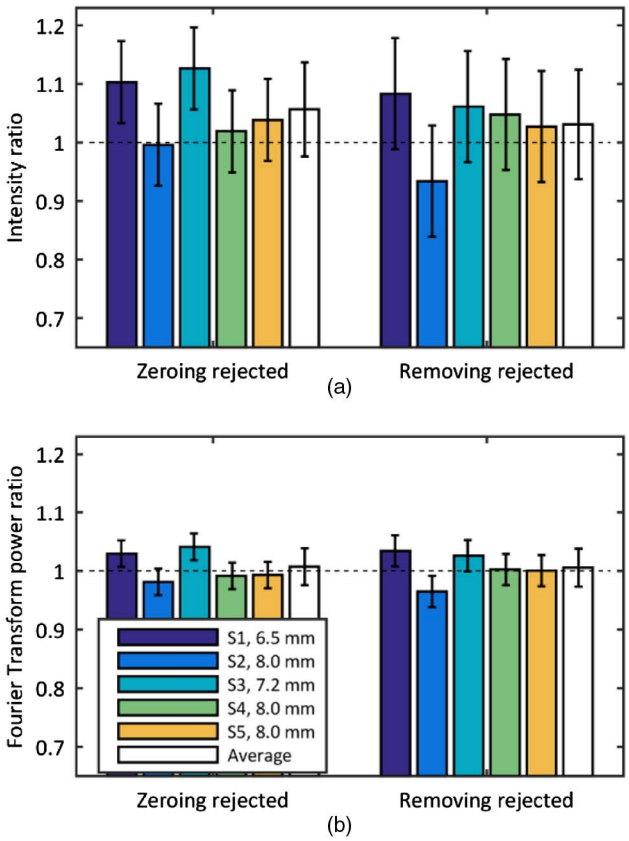


**Fig. 5.** (a) Intensity and (b) frequency content change in the images when controlling a pupil larger than the subject's pupil and rejecting lenslets by either zeroing their slopes (zeroing rejected, left) or removing them from the influence matrix (removing rejected, right). The condition where the pupil size is restricted to the subject's pupil is used as reference. The error bars represent the standard deviation of three repeated measurements.

## 4. DISCUSSION

A spot quality metric combined with neighborhood rules for detecting the pupil boundary allows detection of the pupil using the SH images and improves the practical control of AO retinal imaging in real time. The quality of the retinal images obtained when controlling the wavefront aberration over an area larger than the eye's pupil was similar to the quality of the images obtained when the system's pupil was restricted to an area slightly smaller than the subject's actual pupil. This supports the value of the proposed algorithm for reducing aberrations while still using the maximum pupil size for a given subject without requiring intervention by the experimenter. In principle, this may allow the experimenter, and the system designer, to relax constraints on maintaining head position during imaging, making images more convenient to obtain and increasing the subject's comfort. While we have not implemented a full system with a large system pupil, we have used the algorithm with patients with only a chin rest to good effect. The algorithm also automatically adjusts for drooping eye lids and blinks, as well as irregular pupil shapes.

The use of SH images to track the location and the movement of the pupil has been used previously [9,10]. In our approach, we do not explicitly calculate the movement or the size of the pupil, but rather we directly control for the impact of eye and head motions, as well as pupil size fluctuations, maintaining AO control during the pupil changes. While most AO systems for retinal imaging have an algorithm to deal with the missing spots in the SH and to stop the loop when no light reaches the sensor, the literature on the algorithms used is scarce. In general, there are at least three causes for poor spot formation at the SH sensor. For instance, obscurations of the optics, by the pupil margin or a local obscuration such as cataract, could cause a decrease in the total light in the spot, allowing CCD background noise to dominate the computation of the centroid. Burns [18] proposed setting the slopes of the lenslets at locations with missing or very weak spots to zero, which can help with these types of errors. However, errors in centroids can also arise from scattering or reflections from the cornea or lens. The large depth of field of the SH lenslets can cause these to produce diffuse spots, resulting in an error in centroiding. The edges of the pupil can also cause erroneous slope estimates arising from partial illumination of lenslets, since the slope over part of the lenslet is treated as the average over the entire lenslet. An intensity criterion may not deal with these errors adequately. However, by using a metric based on the ratio between the sum of the intensity of the area surrounding the spot and the sum of the intensity of the whole area corresponding to the lenslet and then applying neighborhood rules to detect the pupil boundary, we can base our wavefront correction on the best data available. This allows robust imaging under a range of imaging conditions. Since these calculations can be performed in each iteration, a snapshot of the visible area of the pupil of the eye is obtained in every iteration of the loop automatically. In principle, this would allow the system to be built with a sufficiently large pupil to include the maximum pupil size across subjects, and the algorithm should quickly accommodate small head movements or eye rotations.

More complex rules are possible, but the two we used that either set the rejected lenslet slope errors to zero and use a constant control matrix, or generate a new control matrix at each iteration of the loop by removing the rows corresponding to the rejected lenslets produced results similar to shrinking the control pupil to match the subject's pupil. In addition, at least for the model eye, convergence speed of the control was not negatively affected for the second method. We did not observe a reliable change in convergence speed for the human subjects, probably because changes in the aberration pattern due to eye movements have a larger impact than the minor improvement in convergence time. It is also important to note that our mirror control algorithm is relatively simple, responding only proportionally to the current error, and not incorporating the rate of change in wavefront error nor long term changes.

The final image quality of the videos in human subjects was quantified using both the average intensities of the images, since in a confocal system the intensity of the images is related to the quality of the AO control [7,11,24] and the area under the image FT up to the cutoff frequency of the average eye's pupil, 135 cycle/deg, obtaining similar results. That is, once converged, all of the algorithms produced equivalent image quality, and thus, the major advantage of the new algorithm was in the ease of use.

We also investigated a more complex control. It has been argued that the intensity of the image of each of the SH spots can be used as a weight (estimating the measurement quality) to obtain a better fit of the wavefront aberration [25]. We implemented a similar approach, but found that in our AO control system, it actually increased convergence times without significantly improving the final image quality. Informally, this seemed to occur because the weighting caused the correction algorithm to first concentrate on the areas of the pupil with the highest pupil metrics and the lowest wavefront errors (i.e., areas with good optical quality, usually in the center of the pupil), and in practice the most important region of the pupil to concentrate correction on are the regions with the largest wavefront errors. We thus also implemented a weighting scheme that was inversely related to the metric, but this did not improve the images, although we implemented only a simple linear relationship between metric and weight, and other relationships may improve the control. Finally, it is important to note that with the current algorithm, the aberrations are not corrected in the areas where the lenslets were rejected, i.e., pupil boundary and obscured areas, and that this may affect the quality of the retinal imaging. Probably an extrapolation of the phase measurements from inside the pupil [11] could further improve the images.

Another possible improvement would be to consider a full model of the impact of the coupling between nearby actuators. It is possible that part of the increased convergence time for zeroing the wavefront error outside the pupil (Fig. 3) is that points outside the eye's pupil are dragging the movement of the DM in areas conjugated to the pupil. The median filter is designed to help with this problem by providing a signal to change actuators around the edges without influencing directly the measurements inside the pupil.

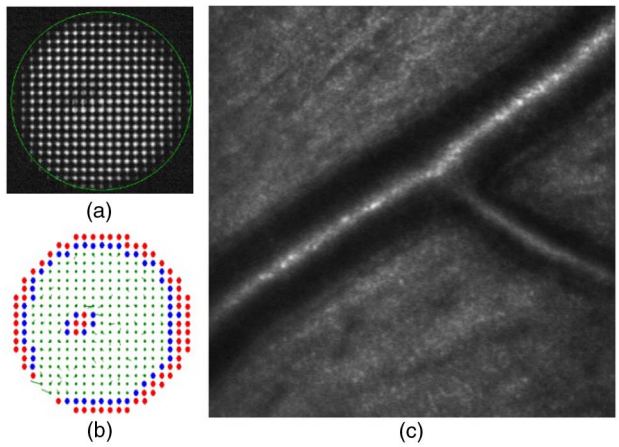


**Fig. 6.** Example of the automatic pupil detection algorithm in a 6-mm diameter pupil diabetic patient with a localized posterior subcapsular cataract. (a) SH image, (b) depending on its metric, rejected spots are marked in red, boundary spots in blue, and accepted lenslets with its local slope are marked in green; (c) retinal imaging showing artery walls.

In the human measurements, we found that a single metric threshold was sufficient for all the subjects, i.e., recalculation of the threshold was not needed for different subjects or when imaging different retinal locations. This threshold could require adjustment in an eye with very low optical quality or in an eye that reflects very little light, but to date this change has not been required. Though we have not performed a rigorous comparison of the results using the algorithm and manually selecting the pupil size, we have used this algorithm with the removing rejected approach to image more than 60 diabetic patients, which included some eyes with intraocular lenses or small cortical or posterior subcapsular cataracts. An example for a patient with a localized subcapsular cataract is shown in Fig. 6, where it can be observed that the regions inside and around the cataract were correctly identified for rejection. While a full clinical investigation is beyond the scope of the current paper, we think that the ability to use whatever portions of the pupil are "good enough" makes this approach promising for clinical applications. In our system, we found that relaxing the need to select the right pupil size and center the pupil on the system helped streamline the collection of images.

One possible limitation of enlarging the field of view of the SH wavefront sensor to sizes larger than the average eye's pupil is that this would imply that, for a given pupil size, fewer lenslets will be used to determine the wavefront error, and a smaller area of the DM would be used for correction. While this can be considered a drawback, error budget studies show that the limiting factor on the AO systems used in ophthalmology is not usually the number of lenslets [26], and technological changes are allowing the construction of DMs with higher numbers of actuators.

**Funding.** National Institute of Health (P30EY019008, R01-EY024315, R01-EY04395); Foundation Fighting Blindness (FFB) (TA-CL-0613-0617-IND).

## REFERENCES


1. J. Liang, D. R. Williams, and D. T. Miller, "Supernormal vision and high-resolution retinal imaging through adaptive optics," J. Opt. Soc. Am. A **14**, 2884–2892 (1997).
2. A. Roorda, F. Romero-Borja, W. Donnelly Iii, H. Queener, T. Hebert, and M. Campbell, "Adaptive optics scanning laser ophthalmoscopy," Opt. Express **10**, 405–412 (2002).
3. B. Hermann, E. J. Fernández, A. Unterhuber, H. Sattmann, A. F. Fercher, W. Drexler, P. M. Prieto, and P. Artal, "Adaptive-optics ultrahigh-resolution optical coherence tomography," Opt. Lett. **29**, 2142–2144 (2004).
4. Y. Zhang, J. Rha, R. Jonnal, and D. Miller, "Adaptive optics parallel spectral domain optical coherence tomography for imaging the living retina," Opt. Express **13**, 4792–4811 (2005).
5. S. Niu, J. Shen, C. Liang, Y. Zhang, and B. Li, "High-resolution retinal imaging with micro adaptive optics system," Appl. Opt. **50**, 4365–4375 (2011).
6. M. Ficocelli and F. B. Amara, "Online tuning of retinal imaging adaptive optics systems," IEEE Trans. Contr. Syst. Technol. **20**, 747–754 (2011).
7. K. Y. Li, S. Mishra, P. Tiruveedhula, and A. Roorda, "Comparison of control algorithms for a MEMS-based adaptive optics scanning laser ophthalmoscope," in *Proceedings of the American Control Conference* (2009), pp. 3848–3853.
8. B. Sahin, B. Lamory, X. Levecq, F. Harms, and C. Dainty, "Adaptive optics with pupil tracking for high resolution retinal imaging," Biomed. Opt. Express **3**, 225–239 (2012).
9. J. Arines, P. Prado, and S. Bará, "Pupil tracking with a Hartmann-Shack wavefront sensor," J. Biomed. Opt. **15**, 036022 (2010).
10. S. Meimon, J. Jarosz, C. Petit, E. G. Salas, K. Grieve, J.-M. Conan, B. Emica, M. Paques, and K. Irsch, "Pupil motion analysis and tracking in ophthalmic systems equipped with wavefront sensing technology," Appl. Opt. **56**, D66–D71 (2017).
11. W. Zou, X. Qi, G. Huang, and S. A. Burns, "Improving wavefront boundary condition for in vivo high resolution adaptive optics ophthalmic imaging," Biomed. Opt. Express **2**, 3309–3320 (2011).
12. C. Miloudi, F. Rossant, I. Bloch, C. Chaumette, A. Leseigneur, J. A. Sahel, S. Meimon, S. Mrejen, and M. Paques, "The negative cone mosaic: a new manifestation of the optical stiles-crawford effect in normal eyes," Invest. Ophthalmol. Visual Sci. **56**, 7043–7050 (2015).
13. R. D. Ferguson, Z. Zhong, D. X. Hammer, M. Mujat, A. H. Patel, C. Deng, W. Zou, and S. A. Burns, "Adaptive optics scanning laser ophthalmoscope with integrated wide-field retinal imaging and tracking," J. Opt. Soc. Am. A **27**, A265–A277 (2010).
14. P. M. Prieto, F. Vargas-Martín, S. Goelz, and P. Artal, "Analysis of the performance of the Hartmann–Shack sensor in the human eye," J. Opt. Soc. Am. A **17**, 1388–1398 (2000).
15. C. Li, N. Sredar, K. M. Ivers, H. Queener, and J. Porter, "A correction algorithm to simultaneously control dual deformable mirrors in a woofer-tweeter adaptive optics system," Opt. Express **18**, 16671–16684 (2010).
16. A. Dubra, "Wavefront sensor and wavefront corrector matching in adaptive optics," Opt. Express **15**, 2762–2769 (2007).
17. S. Marcos, J. S. Werner, S. A. Burns, W. H. Merigan, P. Artal, D. A. Atchison, K. M. Hampson, R. Legras, L. Lundstrom, G. Yoon, J. Carroll, S. S. Choi, N. Doble, A. M. Dubis, A. Dubra, A. Elsner, R. Jonnal, D. T. Miller, M. Paques, H. E. Smithson, L. K. Young, Y. Zhang, M. Campbell, J. Hunter, A. Metha, G. Palczewska, J. Schallek, and L. C. Sincich, "Vision science and adaptive optics, the state of the field," Vision Res. **132**, 3–33 (2017).
18. S. A. Burns, R. Tumbar, A. E. Elsner, D. Ferguson, and D. X. Hammer, "Large-field-of-view, modular, stabilized, adaptive-optics-based scanning laser ophthalmoscope," J. Opt. Soc. Am. A **24**, 1313–1326 (2007).
19. W. Zou, X. Qi, and S. A. Burns, "Woofer-tweeter adaptive optics scanning laser ophthalmoscopic imaging based on Lagrange-multiplier damped least-squares algorithm," Biomed. Opt. Express **2**, 1986–2004 (2011).
20. J. Porter, H. Queener, J. Lin, K. E. Thorn, and A. A. S. Awwal, *Adaptive Optics for Vision Science: Principles, Practices, Design and Applications* (Wiley, 2006).
21. W. Zou, X. Qi, and S. A. Burns, "Wavefront-aberration sorting and correction for a dual-deformable-mirror adaptive-optics system," Opt. Lett. **33**, 2602–2604 (2008).
22. G. Guennebaud and B. Jacob, and others, "Eigen v3," 2010, http://eigen.tuxfamily.org.
23. H. Hofer, L. Chen, G. Y. Yoon, B. Singer, Y. Yamauchi, and D. R. Williams, "Improvement in retinal image quality with dynamic correction of the eye's aberrations," Opt. Express **8**, 631–643 (2001).
24. Y. N. Sulai and A. Dubra, "Non-common path aberration correction in an adaptive optics scanning ophthalmoscope," Biomed. Opt. Express **5**, 3059–3073 (2014).
25. S. I. Panagopoulou and D. R. Neal, "Zonal matrix iterative method for wavefront reconstruction from gradient measurements," J. Refractive Surg. **21**, S563–S569 (2005).
26. J. W. Evans, R. J. Zawadzki, S. M. Jones, S. S. Olivier, and J. S. Werner, "Error budget analysis for an adaptive optics optical coherence tomography system," Opt. Express **17**, 13768–13784 (2009).

# Queries

1. AU: Please check and confirm the acronym “AO” on first occurrence in the Abstract.
2. AU: Please expand the acronym “CCD” on first occurrence.
3. AU: The funding information for this article has been generated using the information you provided to OSA at the time of article submission. Please check it carefully. If any information needs to be corrected or added, please provide the full name of the funding organization/institution as provided in the CrossRef Open Funder Registry (http://www.crossref.org/fundingdata/registry.html).
4. AU: Under “Funding,” should “National Institute of Health” be changed to “National Institutes of Health”?
5. AU: Please provide all author names for Ref. 22, per journal style.

# Supplementary Material

This article has the following supplementary material items associated with it.

1. Visualization 1 Raw SH image (left) and processed image (right) with the rejected lenslets and the pupil boundary marked in red and blue respectively. Changes in the pupil size as well as blinks can be detected in real time.https://doi.org/10.6084/m9.figshare.5229742